ACS NANO

www.acsnano.org

ARTICLE

A Versatile Top-Down Patterning Technique for Perovskite On-Chip Integration

Federico Fabrizi,◆ Saeed Goudarzi,◆ Sana Khan, Tauheed Mohammad, Liudmila Starodubtceva, Piotr J. Cegielski, Felix Thiel, Sercan Özen, Maximilian Schiffer, Felix Lang, Peter Haring Bolívar, Thomas Riedl, Gerhard Müller-Newen, Surendra B. Anantharaman, Maryam Mohammadi,* and Max C. Lemme*

Cite This: *ACS Nano* 2025, 19, 30428−30440

Read Online

ACCESS | Metrics & More | Article Recommendations | Supporting Information

ABSTRACT: **Metal-halide perovskites (MHPs) have exciting optoelectronic properties and are under investigation for various applications, such as photovoltaics, light-emitting diodes, and lasers. An essential step toward exploiting the full potential of this class of materials is their large-scale, on-chip integration with high-resolution, top-down patterning. The development of such patterning methods for perovskite films is challenging because of their intrinsic ionic nature and adverse reactions with the solvents used in standard lithography processes. Here, we introduce a versatile and precise method comprising photolithography and reactive ion etching (RIE) processes that can be tuned to accommodate different perovskite compositions and morphologies. Our method utilizes conventional photoresists at reduced temperatures to create micron-sized features down to 1 μm, providing high reproducibility from chip to chip. The patterning technique is validated through atomic force microscopy (AFM), X-ray diffraction (XRD), optical spectroscopy, and scanning electron microscopy (SEM). It enables the scalable and high-throughput on-chip monolithic integration of MHPs.**

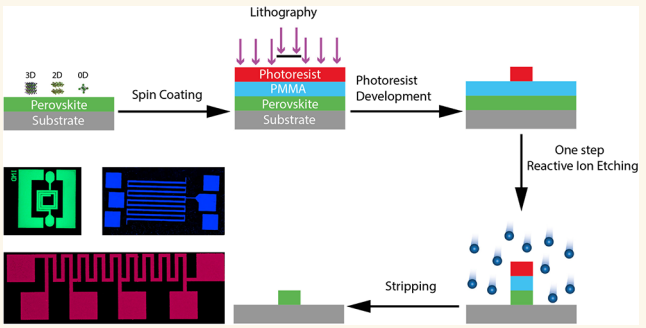

KEYWORDS: *metal-halide perovskites, on-chip integration, top-down patterning, photolithography, reactive ion etching*

INTRODUCTION

Metal-halide perovskites (MHPs) are a class of ionic semiconductors known for their outstanding optoelectronic properties, including charge carrier diffusion lengths exceeding 1 μm[1−4] and tunable bandgap.[5−7] These properties have spawned substantial research in various fields, such as photovoltaics,[8−10] photonics,[11−14] and optoelectronics.[15−19] Furthermore, the optoelectronic properties of MHPs, including their bandgap, exciton binding energy, and charge carrier mobility, depend on both their composition and dimensionality.[5,20] The engineering of the composition of MHPs is facilitated by their rich chemistry, which provides opportunities for tuning their electronic and optical properties.[21,22] Additionally, the dimensionality of MHPs can be altered from three-dimensional (3D)[23] to two-dimensional (2D),[24] one-dimensional (1D),[25] and zero-dimensional (0D).[26]

Technologically, their simple, low-temperature solution-based deposition processes[27] are beneficial for upscaling production once the relevant technology readiness levels are achieved. However, integrated on-chip applications in optoelectronics and photonics, such as displays or light-emitting diodes (LEDs),[28−30] require compatibility with the perovskites' limited thermal budgets and complex semiconductor manufacturing processes.[31−34] One of the key processes for such integration is the patterning of perovskite materials.[35,36] The industry's standard and preferred technique combines top-down photolithography and reactive ion etching (RIE) because of its high resolution, precision, reliability, selectivity, and good cost-performance trade-off. However, traditional photolithography involves wet chemical processing in polar solvents and deionized water, which damages or dissolves highly ionic crystals such as perovskites.[37,38] This chemical instability and sensitivity to polar and protic solvents,[39] which are present in photoresist spin-coating processes, lead to degradation or alteration of the intrinsic

Received: June 21, 2025
Revised: July 23, 2025
Accepted: July 24, 2025
Published: August 12, 2025

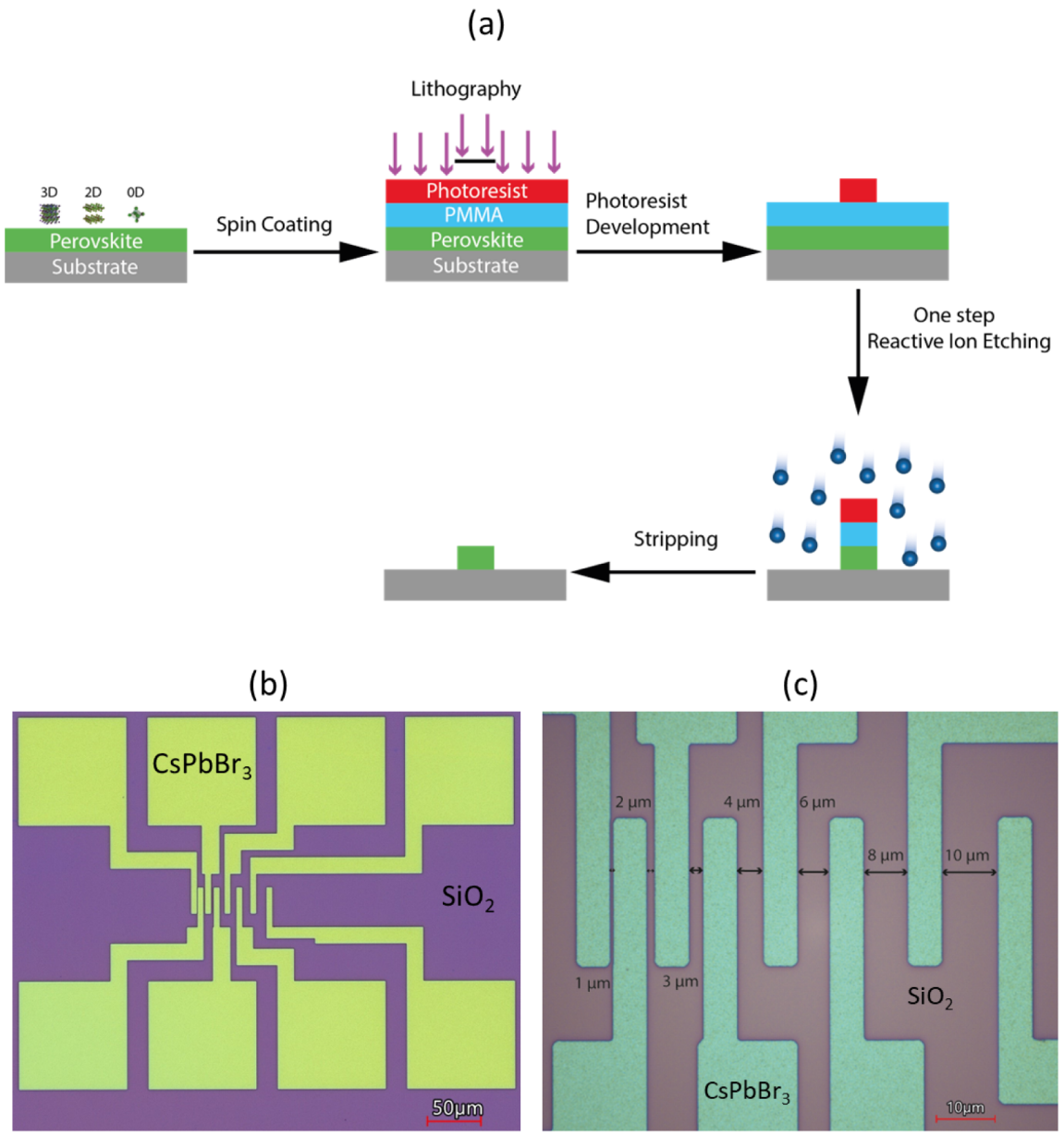

Figure 1. (a) The fabrication process includes the following steps: (1) Deposition of the perovskite thin film (3D, 2D or 0D), (2) deposition of the PMMA layer and the photoactive resist layer (AZ MIR 701), (3) development of the AZ MIR 701 resist layer, (4) pattern transfer into the perovskite layer by reactive ion etching, and (5) stripping by dissolving the bottom resist layer and lifting the top layer. (b, c) Optical microscope image of device features achieved by top-down patterning method with a minimum feature dimension of 1 μm.

properties of the perovskite. Several alternative methods have been developed, such as nanoimprint patterning,[40−43] fluorinated resists,[44] gas-assisted focused ion beam etching,[45] inkjet printing,[46] laser writing[47,48] and wettability-assisted photolithography processes.[49,50] However, these methods do not generally meet the industry's needs for high-speed production on a wafer scale and accurate and consistent features.

Here, we demonstrate a precise and reproducible method for the top-down patterning of perovskite films with micrometer resolution based on standard semiconductor equipment and processes. The micrometer resolution remains highly relevant for a broad range of industrial applications, particularly in emerging technologies involving perovskite-based optoelectronics and hybrid semiconductor devices.[51] In perovskite solar cells,[52] photodetectors,[29,53] light-emitting devices,[54] and lasers[28] feature sizes on the order of 1−10 μm are commonly used. Moreover, UV photolithography at micrometer scales is cost-effective, high-throughput, and compatible with soft perovskite thin films, avoiding possible damage associated with electron beam lithography (EBL) irradiation.[55] While alternative approaches such as nanoimprint lithography (NIL), focused ion beam (FIB), and laser writing can reach submicrometer or nanometer-scale resolution (see Table S1), these methods typically face significant challenges in terms of scalability, processing speed, and compatibility with perovskite materials. The presented method can be tailored for various perovskite types and morphologies, including 3D and low-dimensional (quasi-2D and 0D) structures. We use a double-stack resist composed of poly(methyl methacrylate) (PMMA) and AZ MIR 701, a commercial positive photoresist.[56] The PMMA prevents direct contact between the perovskite and

https://doi.org/10.1021/acsnano.5c10397
ACS Nano 2025, 19, 30428−30440

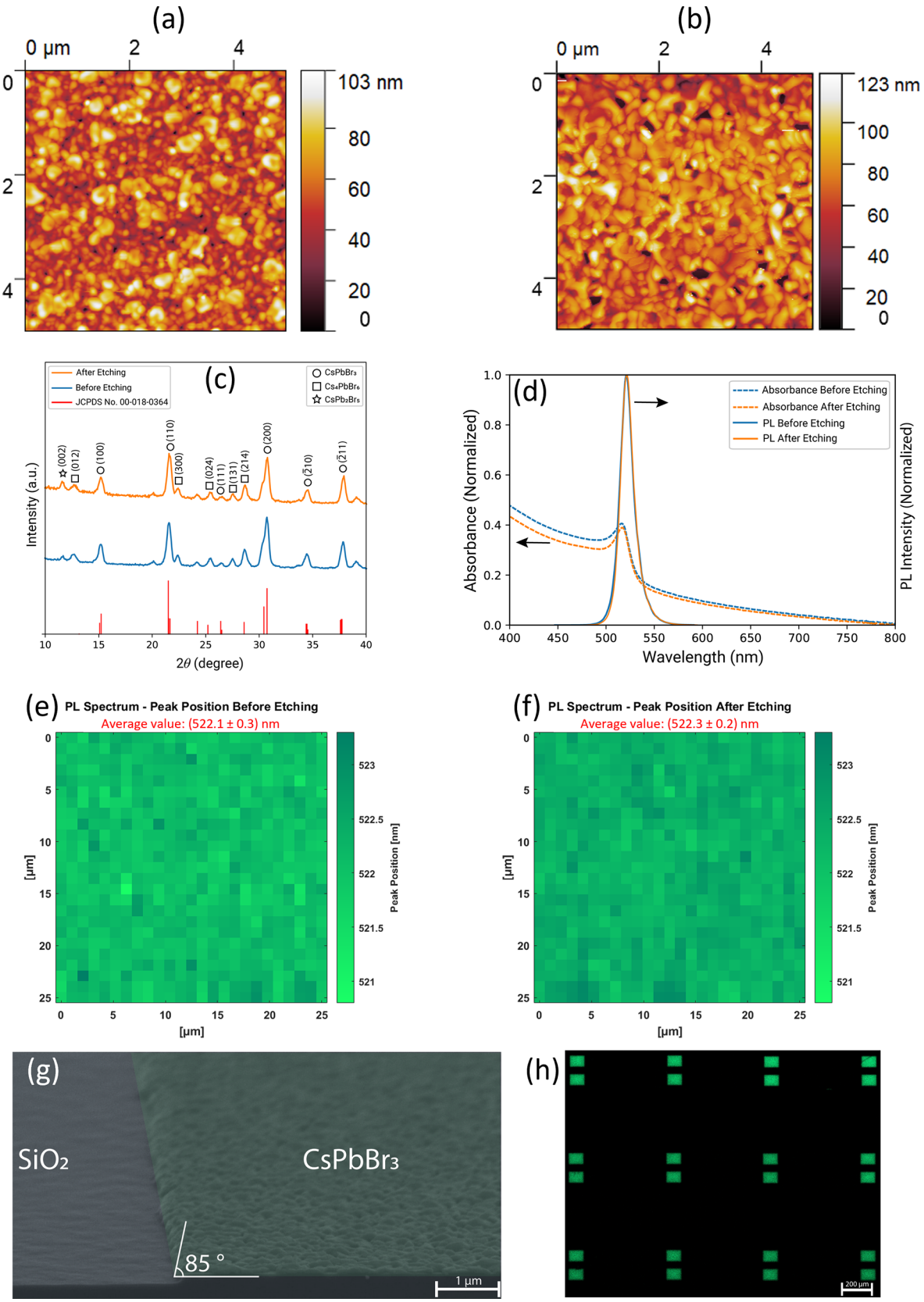

Figure 2. $CsPbBr_3$ patterning. (a) AFM scan of the pristine sample. (b) AFM scan after etching and stripping of the double stack. (c) X-ray diffraction patterns of the samples before and after etching. (d) UV−Vis spectra and PL spectra before and after etching. (e, f) Comparison of PL peak positions before and after etching over an area of 25 μm × 25 μm. (g) Cross-sectional SEM image of the etched structure. (h) Confocal fluorescence microscope image of an array of etched structures.

https://doi.org/10.1021/acsnano.5c10397
ACS Nano 2025, 19, 30428−30440

photoresists,[57] whereas AZ MIR 701 facilitates a standard lithography process. We subsequently employ RIE to etch the perovskites while avoiding oxygen plasma, which also damages the perovskites.[39]

EXPERIMENT

Motivated by earlier works on perovskite-compatible photolithography methods,[28,39,58] we devised a new strategy that integrates two resists and nonoxidative reactive gases into a singular workflow. In the following, we introduce the method and demonstrate its application to 3D cesium lead bromide ($CsPbBr_3$) and methylammonium lead iodide ($MAPbI_3$), quasi-2D ($PEA_2(MAPbBr_3)_{n-1}PbBr_4$) and 0D formamidinium lead bromide ($FAPbBr_3$) perovskites.

The different perovskite thin films were spin-coated onto a Si/SiO_2 substrate (see Experimental Section for more details). A 200 nm encapsulation layer (PMMA) was deposited on top of the perovskite layer via spin-coating at 4000 rpm for 60 s and baking at 80 °C for 10 min. This layer acted as a spacer layer and protected the perovskite material from the photoresist. Then, the AZ MIR 701 photoresist was spin-coated on top of the samples at 3000 rpm for 60 s and soft-baked at 95 °C for 90 s, after which the samples were exposed to ultraviolet (UV) light for 25 s via a contact lithography mask aligner (EVG 420) system. The patterns were developed in MF26A developer for 35 s followed by rinsing for 7 s with deionized water. Then, the samples were etched via a PlasmaLab System 100 inductively coupled plasma (ICP)-RIE tool (Oxford Instruments). All inorganic 3D metal halides, quasi-2D perovskites, and nanocrystalline thin films were etched with radicals from HBr and BCl_3 gases with different gas flows. The hybrid organic−inorganic perovskites were etched with radicals from CF_4, Cl_2 and He gas. Since the metal halide perovskites are sensitive to high temperatures, the etching processes were performed in a step and repeated fashion with one cycle of etching followed by a waiting cycle for 2 min to reduce the substrate temperatures. The etching rate of $CsPbBr_3$ was 100 nm/min, and the selectivity over SiO_2 was 3.6, whereas for $MAPbI_3$, the values were 90 nm/min and 2.7. The etch rate and selectivity over SiO_2 for the quasi-2D perovskite were 95 nm/min and 3.4, and the values for the 0D $FAPbBr_3$ were 92 nm/min and 2.8. Finally, the photoresist stack was removed by dissolving the PMMA encapsulation layer in the nonpolar solvent toluene at 80 °C for 1 h to ensure complete dissolution of the PMMA. A schematic of the process is shown in Figure 1. The process yielded perovskite features as small as 1 μm, which is the smallest resolution achievable with our contact lithography system (Figure 1b,c).

RESULTS AND DISCUSSION

Photolithographic Patterning of Three-Dimensional MHPs. We investigated our process with the 3D perovskites $CsPbBr_3$ and $MAPbI_3$ because they are among the most studied and technologically mature metal halide perovskites.

All-Inorganic Perovskite ($CsPbBr_3$). Figure 2a,b shows atomic force microscopy (AFM) images of the surface topography of the $CsPbBr_3$ thin film before and after etching. The bright areas with greater heights are attributed to the material's secondary phases of $CsPb_2Br_5$ and Cs_4PbBr_6, as evidenced by X-ray diffraction (XRD) measurements (Figure 2c), corroborating previous findings.[13] The root-mean-square (RMS) roughness was 14.92 ± 1.57 nm, which increased to 24.09 ± 1.21 nm after the etching process. We also observed an increase in the average grain size from approximately 65 nm after spin coating to 200 nm after stripping the double-stack resist (Figure S1a,b) and an increase in the number of pinholes in the film. This suggests some degree of recrystallization during the etching process, despite tailoring the etching recipe to limit process-induced heating. It is important to note that derivative phases such as the two-dimensional $CsPb_2Br_5$ and the zero-dimensional Cs_4PbBr_6 can readily convert to the 3D $CsPbBr_3$ phase under post mild thermal treatment, due to their higher thermodynamic stability.[59,60] The AFM images in Figure 2a,b show a reduction in the bright contrast regions corresponding to secondary phases in the pristine film after patterning. The XRD data in Figure 2c show no significant differences in the crystalline phases before and after etching. The spectra show distinct high-intensity peaks at 15.21°, 21.49°, 26.37°, 30.69°, 34.46°, and 37.90°, corresponding to the (100), (110), (111), (200), ($\bar{2}$10), and ($\bar{2}$11) crystallographic planes, respectively, characteristic of monoclinic $CsPbBr_3$ (reference code: JCPDS 00-018-0364).[61,62] Additional peaks were observed at 12.63°, 22.41°, 25.42°, 27.51°, and 28.63°, indicative of the presence of the (012), (300), (024), (131), and (214) crystallographic planes, respectively, associated with the rhombohedral Cs_4PbBr_6 phase.[63] Furthermore, a peak attributed to the (002) plane of the $CsPb_2Br_5$ phase was also observed, supporting the results of the AFM analysis.[64,65] The patterned perovskites were optically characterized through ultraviolet−visible (UV−Vis) absorption and photoluminescence (PL) spectroscopy. The absorption edges before and after the etching process were very similar, approximately 516 and 517 nm, respectively. The photoluminescence peaks remained at 521 nm before and after the etching process, with full widths at half-maximum (FWHM) of 15.1 and 14.9 nm, respectively (see individual spectra in Figure 2d). PL emission maps taken over large scan areas of 25 μm × 25 μm confirmed this result. They are shown in Figure 2e,f, where the color scale indicates the peak position wavelength. The FWHM of the PL spectra also did not change before and after the etching process in the same scanning areas (Figure S1c,d). Moreover, no differences can be discerned in the PL spectra between the center and edges of the etched structures (Figure S1e). Time-resolved photoluminescence measurements were performed before and after etching, and the resulting decay curves were fitted using a double-exponential model (Figure S2). PL decay times τ_1 = 1.39 ns and τ_2 = 4.50 ns for the pristine film (Figure S2a,b), and τ_1 = 1.07 ns and τ_2 = 5.03 ns for the etched sample (Figure S2c,b), were extracted. These results show that etching slightly accelerates the fast decay component (τ_1), likely due to increased surface recombination,[66] while the slower component (τ_2) remains relatively unchanged. This suggests that the optical properties of the material are preserved,[66,67] supporting the potential for device applications after the patterning process. Photoluminescence quantum yield (PLQY) measurements show a slight enhancement from 1.02% to 1.39% after etching (Figure S3).

Figure 2g shows a cross-sectional SEM image of the etched $CsPbBr_3$ sidewall with an angle of approximately 85°. Furthermore, the top-view SEM image, profilometer measurement and optical microscope image after etching in Figure S1f,g and h display low edge roughness and well-defined structures. Confocal fluorescence spectra before and after etching, shown in SI Figure S1i, exhibits the material's

https://doi.org/10.1021/acsnano.5c10397
ACS Nano 2025, 19, 30428−30440

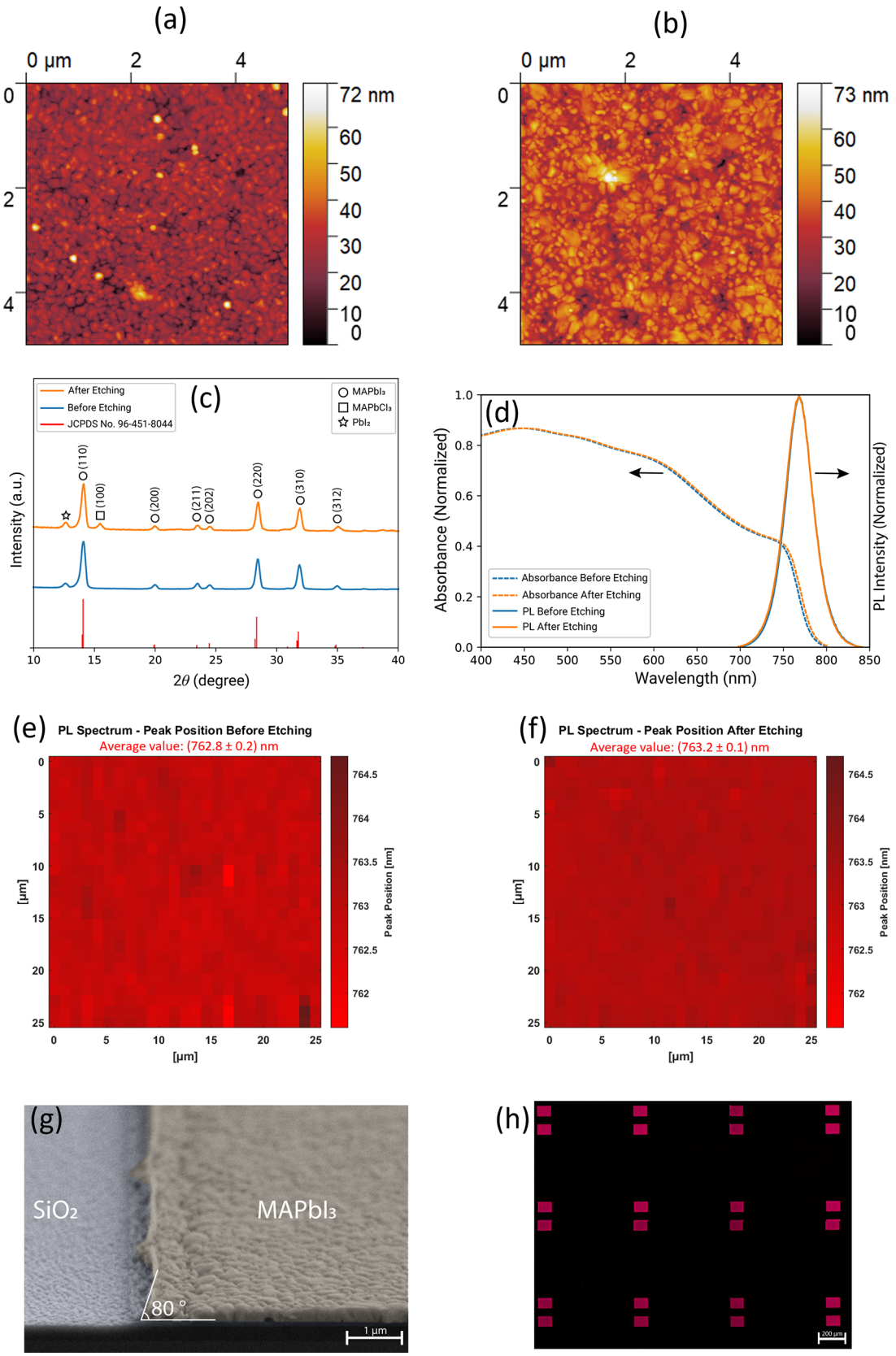

Figure 3. $MAPbI_3$ patterning. (a) AFM scan of the pristine sample. (b) AFM scan after etching and stripping of the double stack. (c) X-ray diffraction patterns of the samples before and after etching. (d) UV−Vis spectra and PL spectra before and after etching. (e, f) Comparison of PL peak positions before and after etching over an area of 25 μm × 25 μm. (g) Cross-sectional SEM image of the etched structure. (h) Confocal fluorescence microscope image of an array of etched structures.

https://doi.org/10.1021/acsnano.5c10397
ACS Nano 2025, 19, 30428−30440

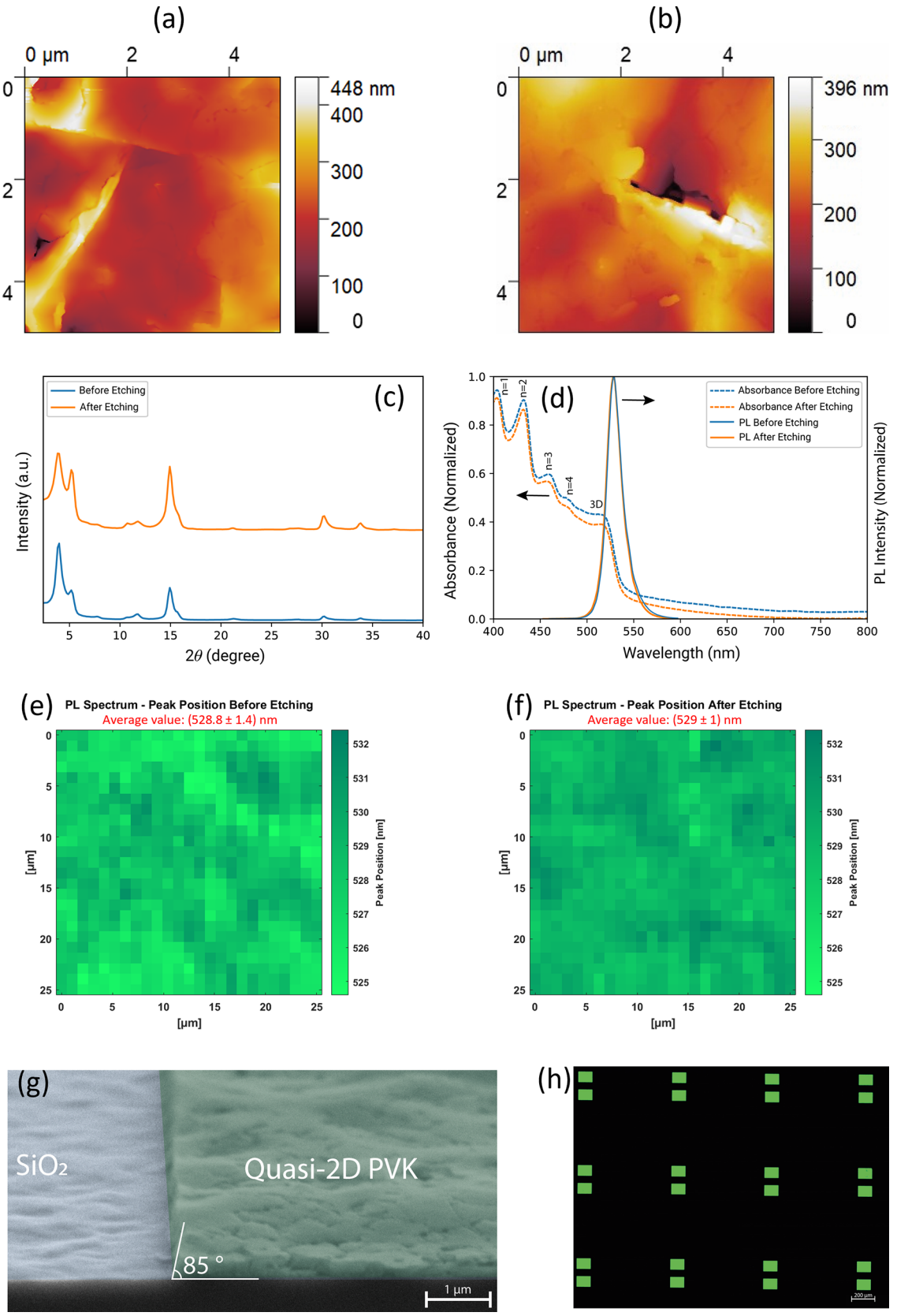

Figure 4. $PEA_2(MAPbBr_3)_{n-1}PbBr_4$ quasi-2D perovskite patterning. (a) AFM scan of the pristine sample. (b) AFM scan after etching and stripping of the double stack. (c) X-ray diffraction patterns of the samples before and after etching. (d) UV−Vis spectra and PL spectra before and after etching. (e,f) Comparison of PL peak positions before and after etching over an area of 25 μm × 25 μm. (g) Cross-sectional SEM image of the etched structure. (h) Confocal fluorescence microscope image of an array of etched structures.

https://doi.org/10.1021/acsnano.5c10397
ACS Nano 2025, 19, 30428−30440

characteristic emission in the green region of the spectrum. The confocal microscopy image of the pristine $CsPbBr_3$ thin film (Figure S1l) and the image after etching (Figure 2h), reveal uniform green fluorescence and display representative patterns that can be achieved through etching. To validate the method's precision, various features fabricated using the developed technique are shown in Figure S4. The applicability of our method to a broader range of all-inorganic perovskite materials, including those with wider band gaps, was confirmed by testing on cesium lead chloride ($CsPbCl_3$) (Figure S5).

Organic–Inorganic Hybrid Perovskite ($MAPbI_3$). We further investigated our etching method with the less stable organometallic halide perovskite $MAPbI_3$, following the same fabrication scheme illustrated in Figure 1.

The morphology of the $MAPbI_3$ thin film before and after etching was examined via AFM (Figure 3a,b). The RMS roughness slightly increased from 6.20 ± 1.99 nm to 7.06 ± 1.08 nm after etching. In contrast to $CsPbBr_3$, there were no noticeable changes in the grain size of $MAPbI_3$. (from 146.85 ± 70.94 nm to 158.64 ± 81.97 nm, Figure S6a,b).

The XRD spectra of $MAPbI_3$ before and after etching have dominant peaks at 14.09°, 19.93°, 23.54°, 24.52°, 28.45°, 31.85°, and 34.9°, corresponding to the (110), (200), (211), (202), (220), (310) and (312) crystallographic planes of the tetragonal phase of $MAPbI_3$, respectively (reference code: JCPDS No. 96-451-8044).[68−72] A minor peak attributed to the PbI_2 phase is also evident at 12.7°.[68] After etching, an additional peak occurred at 15.1°, indicating a different material composition at the edges of the patterned areas. Confocal microscopy images of these areas, compared to the one of the pristine sample (Figure S6c), showed blue and green emissions all over the edges (Figure S6d−f), which can be attributed to halide exchange with chlorine radicals from the etch plasma, resulting in the formation of $MAPbI_{3-x}Cl_x$ ($0 < X \leq 3$).[68] This is enabled by the low crystal formation energy of organic−inorganic hybrid metal halides, facilitating the chloride ion diffusion. UV−Vis absorption and PL spectra of the patterned $MAPbI_3$ structures show absorption edges and photoluminescent peaks at 748 and 768 nm, respectively, and no significant wavelength shifts were observed before and after etching in the sample center (Figure 3d). This is also confirmed by the spectrum extracted from the confocal images (Figure S6g). The FWHM values of 37.4 and 37.2 nm before and after etching, respectively, are comparable. However, the region close to the edge of the $MAPbI_3$ shows a blueshift of approximately 7 nm in the PL peak position (Figure S6h). This can be explained by decreased average grain sizes at the edge of the etched structure (Figure S6i), which also contributed to an enhanced PL intensity (inset of Figure S6h). Similar effects were reported previously for perovskite thin films[28,73] and single crystals.[74] PL maps (Figure 3e,f) and an analysis of the FWHM (Figure S6l,m) over an area of 25 μm × 25 μm in the center of the samples demonstrate the optical stability of $MAPbI_3$ toward the patterning process. To further investigate the impact of the nanofabrication on the luminescence properties, we also conducted PLQY measurements of the pristine $MAPbI_3$ film and after the etching (Figure S7) and observed a reduction from 0.213% to 0.172%. This modest decrease indicates that our nanofabrication process preserves the optical quality of the $MAPbI_3$ film, despite its known sensitivity to processing.

Figure 3g shows a cross-sectional SEM image of the $MAPbI_3$ sidewall with an angle of approximately 80°. Moreover, top-view SEM image, optical microscope image, and profilometer measurement after etching (Figure S6n−p) demonstrate the structured $MAPbI_3$ with a lateral size of 85 μm by 65 μm and a height of 250 nm. Figure 3h shows a confocal microscopy image of typical patterns that can be achieved with $MAPbI_3$, with the characteristic luminescence wavelength in the red range of the spectrum. A diverse set of patterns produced using the proposed technique is shown in Figure S8.

Photolithographic Patterning of Low-Dimensional MHPs. *Quasi-Two-Dimensional Perovskites ($PEA_2(MAPbBr_3)_{n-1}PbBr_4$).* Next, we demonstrated the suitability of the patterning technique in Figure 1 for the fabrication of high-resolution quasi-2D perovskite arrays. AFM images in Figure 4a,b show that the morphology of the perovskites was retained after the process. The roughness of the film slightly decreased from 57.51 ± 8.95 nm to 50.66 ± 15.84 nm, indicating a smoothing effect through the etching process. The XRD spectra in Figure 4c remained unchanged before and after patterning and show four sharp peaks at 5.07°, 14.95°, 21.38°, and 30.20°, corresponding to the (002), (100), (110), and (200) crystal planes of the quasi-2D perovskites, respectively.[75] The low-angle diffraction peak below 5° can be attributed to typical reflections from the layered structure.[76] The UV−Vis and PL spectra in Figure 4d show absorption edges and photoluminescence peaks at 517 and 528 nm, respectively, and no significant peak position shift before and after etching. This is uniform across the sample, as illustrated in the PL emission maps, with only a slight variability of 2 nm in the emission wavelength over an area of 25 μm x 25 μm (Figure 4e,f). An average reduction of approximately 2 nm in the FWHM was observed in area scans (Figure S9a,b). The PL spectra showed no significant differences in emission wavelengths between the center and the edge of the structures (Figure S9c). However, PLQY measurements before and after the etching process (Figure S10) revealed a decrease from 2.11% to 1.56%. Time-resolved photoluminescence measurements showed a biexponential decay for the pristine film, with lifetimes τ_1 = 3.23 ns and τ_2 = 32.48 ns (Figure S11a,b), while the etched sample exhibited τ_1 = 3.34 ns and τ_2 = 47.53 ns (Figure S11c,b). The negligible change in τ_1 after etching (from 3.23 to 3.34 ns) suggests that surface recombination or trap-related losses are not significantly affected by the etching process. In contrast, the notable increase in τ_2 indicates a suppression of nonradiative bulk recombination, possibly due to enhanced passivation during the nanofabrication process.

The cross-sectional SEM image in Figure 4g shows well-defined structures after the etching process, with a sidewall angle of approximately 85°. The quality of the etched $PEA_2(MAPbBr_3)_{n-1}PbBr_4$ structures is shown in Figure S9d−f. The top-view SEM image, optical microscope image, and profilometer measurement after etching illustrate the structured $PEA_2(MAPbBr_3)_{n-1}PbBr_4$ with a lateral size of 85 μm by 65 μm and a height of 290 nm. Confocal fluorescence spectra (Figure S9g) and the corresponding microscopy images (Figures S9h and 4h) show uniform green emission before and after etching. Figure 4h confirms the successful etching of the quasi-2D perovskite with its green emission, with no residual perovskite in the etched area. To demonstrate the versatility of our process, we fabricated several shapes and patterns (Figure S12).

Zero-Dimensional Perovskites ($FAPbBr_3$). Finally, we applied our micropatterning technique to thin films of colloidal $FAPbBr_3$ perovskite nanocrystals (NCs). The surface rough-

https://doi.org/10.1021/acsnano.5c10397
ACS Nano 2025, 19, 30428−30440

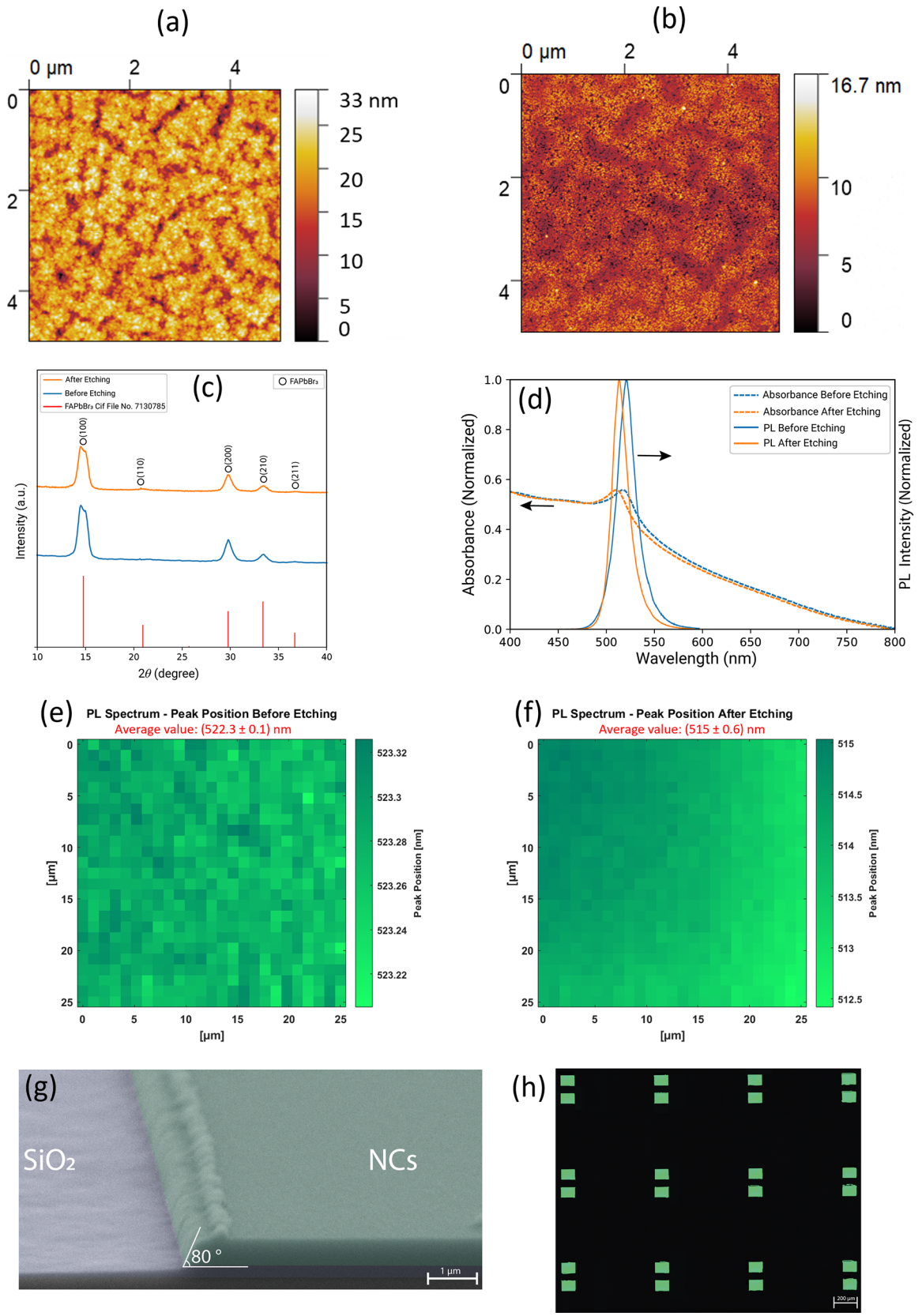

Figure 5. $FAPbBr_3$ patterning. (a) AFM scan map of the pristine sample. (b) AFM scan map after etching and stripping of the double stack. (c) X-ray diffraction patterns of the samples before and after etching. (d) UV−Vis spectra and PL spectra before and after etching. (e, f) Comparison of PL peak positions before and after etching over an area of 25 μm × 25 μm. (g) Cross-sectional SEM image of the etched structure. (h) Confocal fluorescence microscope image of an array of etched structures.

https://doi.org/10.1021/acsnano.5c10397
ACS Nano 2025, 19, 30428−30440

ness of the NC layers was assessed by AFM before and after the etching process (Figure 5a,b), the film roughness decreased from 9.66 ± 0.79 nm to 2.03 ± 0.13 nm. The XRD spectra taken before and after patterning were not significantly affected (Figure 5c), with four characteristic peaks of the cubic structure of $FAPbBr_3$ that correspond to the (100), (110), (200) and (210) crystal planes (.cif file No. 7130785).[77,78] The Scherrer equation $\left(D = \frac{K\lambda}{\beta \cos\theta}\right)$ can be used to measure the size of the nanocrystal. It revealed no significant reduction in the size: 9.66 and 9.12 nm before and after etching, respectively.

The UV−Vis and PL spectra of the NCs exhibited differences in their absorption edges and photoluminescence peaks before and after the etching process. As illustrated in Figure 5d, both spectra show a blueshift of approximately 8 nm after the etching process. The absorption edge before the nanofabrication process was located at 518 nm, whereas it was 510 nm after the etching process. A similar trend was observed for the PL peak position, which moved from 521 to 513 nm. This is confirmed in Figure 5e,f, where an average blueshift of the PL peak position of 8 nm was extracted from the 25 μm × 25 μm area scan. The FWHM before and after etching remained very similar at 19.47 and 19.18 nm, respectively. This was confirmed in the respective area maps (Figure S13a,b). There were also no noticeable differences in the emission peak positions between the center and edge of the etched structure (Figure S13c). Time-resolved photoluminescence measurements revealed similar values for τ_1 before and after etching (τ_1 = 2.63 to 2.49 ns), while showing an increase for τ_2 after etching (τ_2 = 8.65 to 11.37 ns) (Figure S14). PLQY decreased from 51.8% to 11.7% (Figure S15), confirming photoluminescence loss postfabrication, which can be caused by partial ligands removal after the stripping of the double-stack photoresist.

The cross-sectional SEM image in Figure 5g shows well-defined structures after the etching process, with an angle of approximately 80°. Confocal microscopy images show uniform green luminescence from both pristine and structured $FAPbBr_3$ NCs thin films (Figures S13e and 5h, respectively). The blue shift in the PL emission after etching is further confirmed by the confocal fluorescence spectra (Figure S13d). Well-defined regular patterns of NC-based thin films with a thickness of approximately 230 nm (see SEM, optical microscope images and surface profile data in Figure S13f−h. A comparison of the two profilometer line scans before (Figure S13h) and after (Figure S13i) the nanofabrication process revealed a height difference of approximately 20 nm. We attribute this result to the bonding of carboxyl (COOH) groups in PMMA with the unpassivated ionic lead (Pb^{2+}) on the surface,[79] resulting in the lifting of some surface layers of the NCs thin film during the PMMA removal. This could also account for the roughness reduction after the patterning process observed by AFM.

CONCLUSIONS

We developed a top-down patterning technique for metal-halide perovskites based on conventional lithography and reactive ion etching. We demonstrated the method on organic−inorganic hybrids and all-inorganic compounds with different dimensionalities (3D, 2D, and 0D). The technique was evaluated via AFM, XRD, optical spectroscopy, and SEM, confirming that the phase and optical properties of the perovskites were not significantly affected by the patterning process, except at the edges of the patterned organic−inorganic metal halide perovskite. The organometal halide perovskite $MAPbI_3$ showed local halide exchange at the edges of the patterned area with the etching gas ions, which can be explained by its intrinsic soft lattice crystal structure. The developed microstructuring technique showed reproducible results with a resolution down to 1 μm, sufficient for industrial applications where perovskite could potentially be integrated in the future. The UV lithography combined with one step ICP-RIE developed in this work offers a favorable balance of resolution, material compatibility, scalability, and industrial feasibility. The presented approach is applicable on the wafer scale and can achieve high throughput and smaller dimensions with higher-resolution photolithography tools. Therefore, it can be used to monolithically integrate different types of metal-halide perovskites on chip with industry-standard processes. Our technology enables flexible device engineering and can accelerate the research and development of perovskite-based optoelectronics, electronics and energy harvesting applications.

METHODS

Substrates. Si/SiO_2 chips were diced and cleaned from the protective polymer layer by sonication in acetone and isopropanol, followed by 10 min of oxygen plasma cleaning in an RF plasma reactor. The chips were subsequently transferred into a nitrogen-filled glovebox for the perovskite deposition processes.

Perovskite Deposition. All-inorganic perovskite thin films, namely, CsBr (>99.0%, TCI) and $PbBr_2$ (≥98%, Sigma-Aldrich), were combined at a 1:1.7 molar ratio of 14% by weight, dissolved in dimethyl sulfoxide (DMSO, anhydrous, ≥ 99.9%), and then left overnight at 60 °C on a hot plate. The precursor solution was subsequently filtered via 0.20 μm pore size polytetrafluoroethylene (PTFE) filters. Finally, 80 μL of the precursor solution was spin-coated onto the cleaned Si/SiO_2 substrates at 2000 rpm for 40 s, followed by a thermal annealing process at 80 °C for 10 min.

Organic−Inorganic Hybrid Perovskite Thin Films. The $MAPbI_3$ perovskite solution was prepared with 1 M methylammonium (CH_3NH_3I, TCI), lead iodide (PbI_2, 99.999%, Sigma-Aldrich), and dimethyl sulfoxide (DMSO, anhydrous, ≥ 99.9%). These compounds were dissolved in 1 mL of dimethylformamide (DMF, anhydrous, 99.8%) and heated to 60 °C for 1 h while stirring. The resulting solution was then filtered through a 0.20 μm pore size PTFE filter and spin-coated onto the cleaned Si/SiO_2 substrates at 6000 rpm for 30 s. Six seconds after the spin started, 300 μL of chlorobenzene (anhydrous, 99.8%) was added. The resulting film underwent a two-step annealing process (45 °C for 5 min followed by 100 °C for 10 min) to complete the conversion of the precursors into the $MAPbI_3$ perovskite layer.

Quasi-2D Perovskite Thin Films. $PEA_2(MAPbBr_3)_{n-1}PbBr_4$ quasi-2D perovskite thin films were deposited via the spin coating technique. First, the perovskite solution was prepared by dissolving 0.4 mmol of methylammonium bromide (MABr, Sigma-Aldrich), 0.6 mmol lead bromide ($PbBr_2$, TCI), 0.4 mmol phenylethylammonium bromide (PEABr, Sigma-Aldrich), and 0.06 mmol methylammonium chloride (MACl, TCI) in 1 mL of DMSO. The prepared solution was stirred overnight at 60 °C. 80 μL of filtered perovskite solution was spin-coated at 3000 rpm for 2 min and then annealed at 100 °C for 30 min.

Perovskite Nanocrystalline Thin Films. $FAPbBr_3$ NCs were synthesized via a hot-injection method at the Kovalenko laboratory via a previously published protocol.[80] The NC solution was dissolved in cyclohexane at a concentration of approximately 20 mg/mL. The solution was spin-coated at 2400 rpm for 30 s and then at 10000 rpm for 1 s.

Photoluminescence Mapping. Photoluminescence mapping was performed via a WITec confocal Raman microscope (model alpha300R). The samples were scanned with a 457 nm CW laser at 1

https://doi.org/10.1021/acsnano.5c10397
ACS Nano 2025, 19, 30428−30440

μW power. The measurements were taken at room temperature under ambient conditions.

UV−Vis Absorption Spectroscopy. The absorption spectrum of each sample before and after etching was recorded via ultraviolet−visible light spectrophotometry (PerkinElmer Lambda 1050) in the wavelength range of 300 to 800 nm.

AFM, XRD, and SEM Inspection. AFM images were taken from each sample before and after etching via an atomic force microscope (Bruker Dimension Icon) in tapping mode. XRD with filtered Cu−Kα radiation (wavelength at 1.5405 Å) was carried out before and after the etching process via a PANalytical instrument at a current of 40 mA and a voltage of 40 kV. SEM micrographs were taken via an SEM Zeiss SUPRA 60 at 4 kV and a working distance of 3.5 mm.

Confocal Spectral Fluorescence Imaging. Confocal spectral fluorescence imaging was performed with an LSM 710 confocal microscope with a 34-channel Quasar detector (Zeiss, Oberkochen). The samples were excited with a 405 nm diode laser, and the emitted light was collected with an EC Plan-Neofluar 10x/0.30 objective. The microscope system was controlled, and images were acquired in λ mode with the ZEN black software version 2.3 SP1 FP3 (64-bit).

Time-Correlated Single Photon Counting (TCSPC). The Time-Correlated Single Photon Counting (TCSPC) measurement was carried out with a self-constructed measurement system around an inverted microscope (TE300, Nikon). As a scanning system a confocal scan head (PMC2000, Nikon) was used. We have modified the excitation with a pulsed blue laser diode system and the detector with a single photon sensitive photomultiplier system. As excitation a pulsed laser (OEM module, PicoQuant) with a wavelength of 450 nm, a pulse duration below 200 ps, a repetition rate of 10 MHz and an average power of 1 mW was used. The emitted light from the sample was also recorded using the same confocal scan head and then detected using a photomultiplier (PMC 100, Becker & Hickl). For spectral filtering an optical bandpass filter (500−540 nm) was used in the scan head to separate the excitation light from the detection path. Time-correlated single photon counting was performed using a TCSPC measurement card (TimeHarp 200, PicoQuant). To check the homogeneity of the thin films, we used Fluorescence Lifetime Imaging Microscopy (FLIM). Typical image size is 128 by 128 μm^2 with the step size of 1 μm and a temporal resolution of better than 1 ns. The instrument response function (IRF) was measured using scattered laser light and has a full width at half-maximum (FWHM) of 600 ps.

Photoluminescence Quantum Yield (PLQY) Measurements. Absolute Photoluminescence: Excitation for the PL measurements was performed with a 445 nm CW laser (Insaneware) through an optical fiber into an integrating sphere. The intensity of the laser was adjusted to 20 mW/cm^2. A second optical fiber was used from the output of the integrating sphere to an Andor SR393i-B spectrometer equipped with a silicon CCD camera (DU420A-BR-DD, iDus). The system was calibrated by using a calibrated halogen lamp with specified spectral irradiance, which was shone into to integrating sphere. A spectral correction factor was established to match the spectral output of the detector to the calibrated spectral irradiance of the lamp. The spectral photon density was obtained from the corrected detector signal (spectral irradiance) by division by the photon energy (hf), and the photon numbers of the excitation and emission were obtained from numerical integration using Matlab.[81]

ASSOCIATED CONTENT

Supporting Information

r The Supporting Information is available free of charge at https://pubs.acs.org/doi/10.1021/acsnano.5c10397.

Comparison of different photolithographic methods for metal halide perovskites (Table S1); grain size distribution histograms for $CsPbBr_3$ and $MAPbI_3$ thin films; large-area PL mapping, fluorescence and lifetime measurements, and PL quantum yield data for $CsPbBr_3$, $MAPbI_3$, quasi-2D $PEA_2(MAPbBr_3)_{n-1}PbBr_4$, and $FAPbBr_3$ nanocrystals before and after etching; SEM and optical images; PL spectrum comparisons between the centers and edges of etched structures; confocal microscopy images of chloride-, bromide-, and iodide-based perovskite compositions with varied features (PDF)

AUTHOR INFORMATION

Corresponding Authors

Maryam Mohammadi − *AMO GmbH, Aachen 52074, Germany;* orcid.org/0000-0001-9085-0807; Email: mohammadi@amo.de

Max C. Lemme − *AMO GmbH, Aachen 52074, Germany; Chair of Electronic Devices, RWTH Aachen University, Aachen 52074, Germany;* orcid.org/0000-0003-4552-2411; Email: max.lemme@eld.rwth-aachen.de

Authors

Federico Fabrizi − *AMO GmbH, Aachen 52074, Germany; Chair of Electronic Devices, RWTH Aachen University, Aachen 52074, Germany*

Saeed Goudarzi − *Chair of Electronic Devices, RWTH Aachen University, Aachen 52074, Germany*

Sana Khan − *AMO GmbH, Aachen 52074, Germany; Chair of Electronic Devices, RWTH Aachen University, Aachen 52074, Germany*

Tauheed Mohammad − *AMO GmbH, Aachen 52074, Germany;* orcid.org/0000-0001-5815-8407

Liudmila Starodubtceva − *Chair of Electronic Devices, RWTH Aachen University, Aachen 52074, Germany;* orcid.org/0009-0003-0185-4817

Piotr J. Cegielski − *AMO GmbH, Aachen 52074, Germany;* orcid.org/0000-0002-1923-7249

Felix Thiel − *Institute for High Frequency and Quantum Electronics, University of Siegen, Siegen 57076, Germany*

Sercan Özen − *Institute Freigeist Juniorgroup, Radiation Tolerant Electronics with Soft Semiconductors (ROSI), University of Potsdam, Potsdam-Golm 14469, Germany*

Maximilian Schiffer − *Institute of Electronic Devices, University of Wuppertal, Wuppertal 42119, Germany; Wuppertal Center for Smart Materials & Systems (CM@S), University of Wuppertal, Wuppertal 42119, Germany*

Felix Lang − *Institute Freigeist Juniorgroup, Radiation Tolerant Electronics with Soft Semiconductors (ROSI), University of Potsdam, Potsdam-Golm 14469, Germany*

Peter Haring Bolívar − *Institute for High Frequency and Quantum Electronics, University of Siegen, Siegen 57076, Germany;* orcid.org/0000-0001-5875-556X

Thomas Riedl − *Institute of Electronic Devices, University of Wuppertal, Wuppertal 42119, Germany; Wuppertal Center for Smart Materials & Systems (CM@S), University of Wuppertal, Wuppertal 42119, Germany;* orcid.org/0000-0003-1084-316X

Gerhard Müller-Newen − *Institute of Biochemistry and Molecular Biology, Uniklinik RWTH Aachen, Aachen 52074, Germany*

Surendra B. Anantharaman − *AMO GmbH, Aachen 52074, Germany; Low-dimensional Semiconductors Lab, Department of Metallurgical and Materials Engineering, Indian Institute of Technology Madras, Chennai 600036, India;* orcid.org/0000-0002-1882-5540

Complete contact information is available at:

https://doi.org/10.1021/acsnano.5c10397
ACS Nano 2025, 19, 30428−30440

https://pubs.acs.org/10.1021/acsnano.5c10397

Author Contributions

◆F.F. and S.G. contributed equally.

Notes

The authors declare no competing financial interest.

ACKNOWLEDGMENTS

This project has been funded by Deutsche Forschungsgemeinschaft within TRR 404 Active-3D (project number: 528378584), European Union's Horizon 2020 research and innovation programme under the Marie Skłodowska-Curie grant agreement No 956270, the project FOXES (951774), the German Research Foundation (DFG) through the project Hiper-Lase (GI 1145/4-1, LE 2440/12-1, HA 3022/13-1 and RI 1551/18-1) and RI 1551/22-1, and the German Ministry of Education and Research (BMBF) through the project NEPOMUQ (13N17112 and 13N17113). This work was also supported by the Confocal Microscopy Facility, a Core Facility of the Interdisciplinary Center for Clinical Research (IZKF) Aachen within the Faculty of Medicine at RWTH Aachen University. F.L. and S.Ö. thank the Volkswagen Foundation for Funding via the Freigeist Program. S.B.A. acknowledges the New Faculty Initiation Grant (RF23240771MMNFIG009054) from the Indian Institute of Technology Madras, India. T.M. acknowledges IGSTC Post-Doctoral Industrial Fellowship (PDIF) – 2021, Project File No. IGSTC/IF Call 2021/PDIF – (TM)/27/2021-22/. The authors thank P. Grewe and Dr. U. Böttger (Electronic Material Research Lab, RWTH Aachen University) for their support in the XRD measurements. The authors thank Dr. V. Morad and Prof. Dr. M. Kovalenko (ETH Zurich) for providing the perovskite nanocrystals.

REFERENCES

(1) Stranks, S. D.; Eperon, G. E.; Grancini, G.; Menelaou, C.; Alcocer, M. J. P.; Leijtens, T.; Herz, L. M.; Petrozza, A.; Snaith, H. J. Electron-Hole Diffusion Lengths Exceeding 1 Micrometer in an Organometal Trihalide Perovskite Absorber. *Science* **2013**, *342* (6156), 341–344.

(2) Delor, M.; Slavney, A. H.; Wolf, N. R.; Filip, M. R.; Neaton, J. B.; Karunadasa, H. I.; Ginsberg, N. S. Carrier Diffusion Lengths Exceeding 1 Mm Despite Trap-Limited Transport in Halide Double Perovskites. *ACS Energy Lett.* **2020**, *5* (5), 1337–1345.

(3) Xiao, R.; Hou, Y.; Fu, Y.; Peng, X.; Wang, Q.; Gonzalez, E.; Jin, S.; Yu, D. Photocurrent Mapping in Single-Crystal Methylammonium Lead Iodide Perovskite Nanostructures. *Nano Lett.* **2016**, *16* (12), 7710–7717.

(4) Lim, J.; Kober-Czerny, M.; Lin, Y.-H.; Ball, J. M.; Sakai, N.; Duijnstee, E. A.; Hong, M. J.; Labram, J. G.; Wenger, B.; Snaith, H. J. Long-Range Charge Carrier Mobility in Metal Halide Perovskite Thin-Films and Single Crystals via Transient Photo-Conductivity. *Nat. Commun.* **2022**, *13* (1), 4201.

(5) Manser, J. S.; Christians, J. A.; Kamat, P. V. Intriguing Optoelectronic Properties of Metal Halide Perovskites. *Chem. Rev.* **2016**, *116* (21), 12956–13008.

(6) Tao, S. X.; Cao, X.; Bobbert, P. A. Accurate and Efficient Band Gap Predictions of Metal Halide Perovskites Using the DFT-1/2 Method: GW Accuracy with DFT Expense. *Sci. Rep.* **2017**, *7* (1), 14386.

(7) Ou, Q.; Bao, X.; Zhang, Y.; Shao, H.; Xing, G.; Li, X.; Shao, L.; Bao, Q. Band Structure Engineering in Metal Halide Perovskite Nanostructures for Optoelectronic Applications. *Nano Mater. Sci.* **2019**, *1* (4), 268–287.

(8) Liu, S.; Lu, Y.; Yu, C.; Li, J.; Luo, R.; Guo, R.; Liang, H.; Jia, X.; Guo, X.; Wang, Y.-D.; et al. Triple-Junction Solar Cells with Cyanate in Ultrawide Bandgap Perovskites. *Nature* **2024**, *628*, 306–312.

(9) Green, M. A.; Dunlop, E. D.; Yoshita, M.; Kopidakis, N.; Bothe, K.; Siefer, G.; Hao, X. Solar Cell Efficiency Tables (Version 62). *Prog. Photovolt: Res. Appl.* **2023**, *31* (7), 651–663.

(10) Brinkmann, K. O.; Becker, T.; Zimmermann, F.; Kreusel, C.; Gahlmann, T.; Theisen, M.; Haeger, T.; Olthof, S.; Tückmantel, C.; Günster, M.; Maschwitz, T.; Göbelsmann, F.; Koch, C.; Hertel, D.; Caprioglio, P.; Peña-Camargo, F.; Perdigón-Toro, L.; Al-Ashouri, A.; Merten, L.; Hinderhofer, A.; Gomell, L.; Zhang, S.; Schreiber, F.; Albrecht, S.; Meerholz, K.; Neher, D.; Stolterfoht, M.; Riedl, T. Perovskite–Organic Tandem Solar Cells with Indium Oxide Interconnect. *Nature* **2022**, *604* (7905), 280–286.

(11) Wang, Y.; Fan, Y.; Zhang, X.; Tang, H.; Song, Q.; Han, J.; Xiao, S. Highly Controllable Etchless Perovskite Microlasers Based on Bound States in the Continuum. *ACS Nano* **2021**, *15* (4), 7386–7391.

(12) Huang, C.; Zhang, C.; Xiao, S.; Wang, Y.; Fan, Y.; Liu, Y.; Zhang, N.; Qu, G.; Ji, H.; Han, J.; Ge, L.; Kivshar, Y.; Song, Q. Ultrafast Control of Vortex Microlasers. *Science* **2020**, *367* (6481), 1018–1021.

(13) Pourdavoud, N.; Haeger, T.; Mayer, A.; Cegielski, P. J.; Giesecke, A. L.; Heiderhoff, R.; Olthof, S.; Zaefferer, S.; Shutsko, I.; Henkel, A.; et al. Room-Temperature Stimulated Emission and Lasing in Recrystallized Cesium Lead Bromide Perovskite Thin Films. *Adv. Mater.* **2019**, *31* (39), 1903717.

(14) Sun, W.; Liu, Y.; Qu, G.; Fan, Y.; Dai, W.; Wang, Y.; Song, Q.; Han, J.; Xiao, S. Lead Halide Perovskite Vortex Microlasers. *Nat. Commun.* **2020**, *11* (1), 4862.

(15) Yuan, F.; Folpini, G.; Liu, T.; Singh, U.; Treglia, A.; Lim, J. W. M.; Klarbring, J.; Simak, S. I.; Abrikosov, I. A.; Sum, T. C.; Petrozza, A.; Gao, F. Bright and Stable Near-Infrared Lead-Free Perovskite Light-Emitting Diodes. *Nat. Photonics* **2024**, *18* (2), 170–176.

(16) Elkhouly, K.; Goldberg, I.; Zhang, X.; Annavarapu, N.; Hamdad, S.; Croes, G.; Rolin, C.; Genoe, J.; Qiu, W.; Gehlhaar, R.; Heremans, P. Electrically Assisted Amplified Spontaneous Emission in Perovskite Light-Emitting Diodes. *Nat. Photonics* **2024**, *18* (2), 132–138.

(17) Zhao, H.; Chen, H.; Bai, S.; Kuang, C.; Luo, X.; Teng, P.; Yin, C.; Zeng, P.; Hou, L.; Yang, Y.; Duan, L.; Gao, F.; Liu, M. High-Brightness Perovskite Light-Emitting Diodes Based on FAPbBr3 Nanocrystals with Rationally Designed Aromatic Ligands. *ACS Energy Lett.* **2021**, *6* (7), 2395–2403.

(18) Liu, X.-K.; Xu, W.; Bai, S.; Jin, Y.; Wang, J.; Friend, R. H.; Gao, F. Metal Halide Perovskites for Light-Emitting Diodes. *Nat. Mater.* **2021**, *20* (1), 10–21.

(19) Bai, W.; Xuan, T.; Zhao, H.; Dong, H.; Cheng, X.; Wang, L.; Xie, R.-J. Perovskite Light-Emitting Diodes with an External Quantum Efficiency Exceeding 30%. *Adv. Mater.* **2023**, *35* (39), 2302283.

(20) Hoye, R. L. Z.; Hidalgo, J.; Jagt, R. A.; Correa-Baena, J.-P.; Fix, T.; MacManus-Driscoll, J. L. The Role of Dimensionality on the Optoelectronic Properties of Oxide and Halide Perovskites, and Their Halide Derivatives. *Adv. Energy Mater.* **2022**, *12* (4), 2100499.

(21) Filip, M. R.; Eperon, G. E.; Snaith, H. J.; Giustino, F. Steric Engineering of Metal-Halide Perovskites with Tunable Optical Band Gaps. *Nat. Commun.* **2014**, *5* (1), 5757.

(22) Akkerman, Q. A.; D'Innocenzo, V.; Accornero, S.; Scarpellini, A.; Petrozza, A.; Prato, M.; Manna, L. Tuning the Optical Properties of Cesium Lead Halide Perovskite Nanocrystals by Anion Exchange Reactions. *J. Am. Chem. Soc.* **2015**, *137* (32), 10276–10281.

(23) Li, X.; Aftab, S.; Hussain, S.; Kabir, F.; Henaish, A. M. A.; Al-Sehemi, A. G.; Pallavolu, M. R.; Koyyada, G. Dimensional Diversity (0D, 1D, 2D, and 3D) in Perovskite Solar Cells: Exploring the Potential of Mixed-Dimensional Integrations. *J. Mater. Chem. A* **2024**, *12* (8), 4421–4440.

(24) Mao, L.; Stoumpos, C. C.; Kanatzidis, M. G. Two-Dimensional Hybrid Halide Perovskites: Principles and Promises. *J. Am. Chem. Soc.* **2019**, *141* (3), 1171–1190.

(25) Yuan, Z.; Zhou, C.; Tian, Y.; Shu, Y.; Messier, J.; Wang, J. C.; van de Burgt, L. J.; Kountouriotis, K.; Xin, Y.; Holt, E.; et al. One-Dimensional Organic Lead Halide Perovskites with Efficient Bluish White-Light Emission. *Nat. Commun.* **2017**, *8* (1), 14051.
(26) Kahwagi, R. F.; Thornton, S. T.; Smith, B.; Koleilat, G. I. Dimensionality Engineering of Metal Halide Perovskites. *Front Optoelectron.* **2020**, *13* (3), 196−224.
(27) Calisi, N.; Galvanetto, E.; Borgioli, F.; Martinuzzi, S. M.; Bacci, T.; Caporali, S. Thin Films Deposition of Fully Inorganic Metal Halide Perovskites: A Review. *Mater. Sci. Semicond. Process.* **2022**, *147*, 106721.
(28) Cegielski, P. J.; Giesecke, A. L.; Neutzner, S.; Porschatis, C.; Gandini, M.; Schall, D.; Perini, C. A. R.; Bolten, J.; Suckow, S.; Kataria, S.; Chmielak, B.; Wahlbrink, T.; Petrozza, A.; Lemme, M. C. Monolithically Integrated Perovskite Semiconductor Lasers on Silicon Photonic Chips by Scalable Top-Down Fabrication. *Nano Lett.* **2018**, *18* (11), 6915−6923.
(29) Xu, Z.; Han, X.; Wu, W.; Li, F.; Wang, R.; Lu, H.; Lu, Q.; Ge, B.; Cheng, N.; Li, X.; et al. Controlled On-Chip Fabrication of Large-Scale Perovskite Single Crystal Arrays for High-Performance Laser and Photodetector Integration. *Light: Sci. Appl.* **2023**, *12* (1), 67.
(30) Jastrzebska-Perfect, P.; Zhu, W.; Saravanapavanantham, M.; Li, Z.; Spector, S. O.; Brenes, R.; Satterthwaite, P. F.; Ram, R. J.; Niroui, F. On-Site Growth of Perovskite Nanocrystal Arrays for Integrated Nanodevices. *Nat. Commun.* **2023**, *14* (1), 3883.
(31) Liu, Y.; Gao, C.; Li, D.; Zhang, X.; Zhu, J.; Wu, M.; Liu, W.; Shi, T.; He, X.; Wang, J.; et al. Dynamic X-Ray Imaging with Screen-Printed Perovskite CMOS Array. *Nat. Commun.* **2024**, *15* (1), 1588.
(32) Deumel, S.; van Breemen, A.; Gelinck, G.; Peeters, B.; Maas, J.; Verbeek, R.; Shanmugam, S.; Akkerman, H.; Meulenkamp, E.; Huerdler, J. E.; Acharya, M.; García-Batlle, M.; Almora, O.; Guerrero, A.; Garcia-Belmonte, G.; Heiss, W.; Schmidt, O.; Tedde, S. F. High-Sensitivity High-Resolution X-Ray Imaging with Soft-Sintered Metal Halide Perovskites. *Nat. Electron.* **2021**, *4* (9), 681−688.
(33) Hou, Y.; Li, J.; Yoon, J.; Knoepfel, A. M.; Yang, D.; Zheng, L.; Ye, T.; Ghosh, S.; Priya, S.; Wang, K. Retina-Inspired Narrowband Perovskite Sensor Array for Panchromatic Imaging. *Sci. Adv.* **2023**, *9* (15), No. eade2338.
(34) Li, Y.; Jiang, X.; Chen, Y.; Wang, Y.; Wu, Y.; Yu, D.; Wang, K.; Bai, S.; Xiao, S.; Song, Q. A Platform for Integrated Spectrometers Based on Solution-Processable Semiconductors. *Light: Sci. Appl.* **2023**, *12* (1), 184.
(35) Soci, C.; Adamo, G.; Cortecchia, D.; Wang, K.; Xiao, S.; Song, Q.; Schall-Giesecke, A. L.; Cegielski, P. J.; Lemme, M. C.; Gerace, D.; Sanvitto, D.; Tian, J.; Tonkaev, P. A.; Makarov, S. V.; Kivshar, Y. S.; Jimenez Gordillo, O. A.; Melloni, A.; Pushkarev, A. P.; D'Amato, M.; Lhuillier, E.; Bramati, A. Roadmap on Perovskite Nanophotonics. *Opt. Mater.: X* **2023**, *17*, 100214.
(36) Wu, S.; Chen, Z.; Yip, H.-L.; Jen, A. K.-Y. The Evolution and Future of Metal Halide Perovskite-Based Optoelectronic Devices. *Matter* **2021**, *4* (12), 3814−3834.
(37) Bisquert, J.; Juarez-Perez, E. J. The Causes of Degradation of Perovskite Solar Cells. *J. Phys. Chem. Lett.* **2019**, *10* (19), 5889−5891.
(38) Kye, Y.-H.; Yu, C.-J.; Jong, U.-G.; Chen, Y.; Walsh, A. Critical Role of Water in Defect Aggregation and Chemical Degradation of Perovskite Solar Cells. *J. Phys. Chem. Lett.* **2018**, *9* (9), 2196−2201.
(39) Harwell, J.; Burch, J.; Fikouras, A.; Gather, M. C.; Di Falco, A.; Samuel, I. D. W. Patterning Multicolor Hybrid Perovskite Films via Top-Down Lithography. *ACS Nano* **2019**, *13* (4), 3823−3829.
(40) Pourdavoud, N.; Wang, S.; Mayer, A.; Hu, T.; Chen, Y.; Marianovich, A.; Kowalsky, W.; Heiderhoff, R.; Scheer, H.-C.; Riedl, T. Photonic Nanostructures Patterned by Thermal Nanoimprint Directly into Organo-Metal Halide Perovskites. *Adv. Mater.* **2017**, *29* (12), 1605003.
(41) Mayer, A.; Haeger, T.; Runkel, M.; Staabs, J.; Rond, J.; van Gen Hassend, F.; Görrn, P.; Riedl, T.; Scheer, H.-C. Direct Patterning of Methylammonium Lead Bromide Perovskites by Thermal Imprint. *Appl. Phys. A: Mater. Sci. Process.* **2022**, *128* (5), 399.
(42) Muscarella, L. A.; Cordaro, A.; Krause, G.; Pal, D.; Grimaldi, G.; Antony, L. S. D.; Langhorst, D.; Callies, A.; Bläsi, B.; Höhn, O.; Koenderink, A. F.; Polman, A.; Ehrler, B. Nanopatterning of Perovskite Thin Films for Enhanced and Directional Light Emission. *ACS Appl. Mater. Interfaces* **2022**, *14* (33), 38067−38076.
(43) He, X.; Liu, P.; Zhang, H.; Liao, Q.; Yao, J.; Fu, H. Patterning Multicolored Microdisk Laser Arrays of Cesium Lead Halide Perovskite. *Adv. Mater.* **2017**, *29* (12), 1604510.
(44) Lin, C. H.; Zeng, Q.; Lafalce, E.; Yu, S.; Smith, M. J.; Yoon, Y. J.; Chang, Y.; Jiang, Y.; Lin, Z.; Vardeny, Z. V.; Tsukruk, V. V. Large-Area Lasing and Multicolor Perovskite Quantum Dot Patterns. *Adv. Opt. Mater.* **2018**, *6* (16), 1800474.
(45) Alias, M. S.; Yang, Y.; Ng, T. K.; Dursun, I.; Shi, D.; Saidaminov, M. I.; Priante, D.; Bakr, O. M.; Ooi, B. S. Enhanced Etching, Surface Damage Recovery, and Submicron Patterning of Hybrid Perovskites Using a Chemically Gas-Assisted Focused-Ion Beam for Subwavelength Grating Photonic Applications. *J. Phys. Chem. Lett.* **2016**, *7* (1), 137−142.
(46) Zhu, M.; Duan, Y.; Liu, N.; Li, H.; Li, J.; Du, P.; Tan, Z.; Niu, G.; Gao, L.; Huang, Y.; et al. Electrohydrodynamically Printed High-Resolution Full-Color Hybrid Perovskites. *Adv. Funct. Mater.* **2019**, *29* (35), 1903294.
(47) Shishkin, I.; Polushkin, A.; Tiguntseva, E.; Murzin, A.; Stroganov, B.; Kapitonov, Y.; Kulinich, S. A.; Kuchmizhak, A.; Makarov, S. Single-Step Direct Laser Writing of Halide Perovskite Microlasers. *Appl. Phys. Express* **2019**, *12* (12), 122001.
(48) Chen, J.; Wu, Y.; Li, X.; Cao, F.; Gu, Y.; Liu, K.; Liu, X.; Dong, Y.; Ji, J.; Zeng, H. Simple and Fast Patterning Process by Laser Direct Writing for Perovskite Quantum Dots. *Adv. Mater. Technol.* **2017**, *2* (10), 1700132.
(49) Wu, J.; Chen, J.; Zhang, Y.; Xu, Z.; Zhao, L.; Liu, T.; Luo, D.; Yang, W.; Chen, K.; Hu, Q.; Ye, F.; Wu, P.; Zhu, R.; Gong, Q. Pinhole-Free Hybrid Perovskite Film with Arbitrarily-Shaped Micro-Patterns for Functional Optoelectronic Devices. *Nano Lett.* **2017**, *17* (6), 3563−3569.
(50) Lee, W.; Lee, J.; Yun, H.; Kim, J.; Park, J.; Choi, C.; Kim, D. C.; Seo, H.; Lee, H.; Yu, J. W.; Lee, W. B.; Kim, D.-H. High-Resolution Spin-on-Patterning of Perovskite Thin Films for a Multiplexed Image Sensor Array. *Adv. Mater.* **2017**, *29* (40), 1702902.
(51) Liao, K.; Lian, Y.; Yu, M.; Du, Z.; Dai, T.; Wang, Y.; Yan, H.; Wang, S.; Lu, C.; Chan, C. T.; Zhu, R.; Di, D.; Hu, X.; Gong, Q. Hetero-Integrated Perovskite/Si3N4 on-Chip Photonic System. *Nat. Photonics* **2025**, *19* (4), 358−368.
(52) Prince, K. J.; Muzzillo, C. P.; Mirzokarimov, M.; Wolden, C. A.; Wheeler, L. M. All-Back-Contact Perovskite Solar Cells Using Cracked Film Lithography. *ACS Appl. Energy Mater.* **2022**, *5* (8), 9273−9279.
(53) Hu, G.; Guo, J.; Jiang, J.; Wang, L.; Zhang, J.; Chen, H.; Lou, G.; Wei, W.; Shen, L. Capillary Condensation-Driven Growth of Perovskite Nanowire Arrays for Multi-Functional Photodetector. *Light: Sci. Appl.* **2025**, *14* (1), 61.
(54) Yuan, M.; Feng, J.; Li, H.; Gao, H.; Qiu, Y.; Jiang, L.; Wu, Y. Remote Epitaxial Crystalline Perovskites for Ultrahigh-Resolution Micro-LED Displays. *Nat. Nanotechnol.* **2025**, *20* (3), 381−387.
(55) Jin, B.; Zhao, D.; Liang, F.; Liu, L.; Liu, D.; Wang, P.; Qiu, M. Electron-Beam Irradiation Induced Regulation of Surface Defects in Lead Halide Perovskite Thin Films. *Research* **2021**.
(56) Microchemicals Gmb, *AZ MIR 701 Photoresist (29 CPS) - 0.25 l*. https://www.microchemicals.com/AZ-MIR-701-Photoresist-29-CPS-0.25-l/1701290250 (Accessed 23 July 2025).
(57) Zhang, N.; Sun, W.; Rodrigues, S. P.; Wang, K.; Gu, Z.; Wang, S.; Cai, W.; Xiao, S.; Song, Q. Highly Reproducible Organometallic Halide Perovskite Microdevices Based on Top-Down Lithography. *Adv. Mater.* **2017**, *29* (15), 1606205.
(58) Zou, C.; Chang, C.; Sun, D.; Böhringer, K. F.; Lin, L. Y. Photolithographic Patterning of Perovskite Thin Films for Multicolor Display Applications. *Nano Lett.* **2020**, *20* (5), 3710−3717.
(59) Tong, G.; Jiang, M.; Son, D.-Y.; Qiu, L.; Liu, Z.; Ono, L. K.; Qi, Y. Inverse Growth of Large-Grain-Size and Stable Inorganic

Perovskite Micronanowire Photodetectors. *ACS Appl. Mater. Interfaces* **2020**, *12* (12), 14185−14194.
(60) Nasi, L.; Calestani, D.; Mezzadri, F.; Mariano, F.; Listorti, A.; Ferro, P.; Mazzeo, M.; Mosca, R. All-Inorganic CsPbBr3 Perovskite Films Prepared by Single Source Thermal Ablation. *Front. Chem.* **2020**, *8*, 313.
(61) Xu, D.; Wan, Q.; Wu, S.; Zhao, Y.; Xu, X.; Li, L.; He, G. Enhancing the Performance of LARP-Synthesized CsPbBr3 Nanocrystal LEDs by Employing a Dual Hole Injection Layer. *RSC Adv.* **2020**, *10* (30), 17653−17659.
(62) Gou, Z.; Huanglong, S.; Ke, W.; Sun, H.; Tian, H.; Gao, X.; Zhu, X.; Yang, D.; Wangyang, P. Self-Powered X-Ray Detector Based on All-Inorganic Perovskite Thick Film with High Sensitivity Under Low Dose Rate. *Phys. Status Solidi RRL* **2019**, *13* (8), 1900094.
(63) Yang, L.; Li, D.; Wang, C.; Yao, W.; Wang, H.; Huang, K. Room-Temperature Synthesis of Pure Perovskite-Related Cs4PbBr6 Nanocrystals and Their Ligand-Mediated Evolution into Highly Luminescent CsPbBr3 Nanosheets. *J. Nanopart. Res.* **2017**, *19* (7), 258.
(64) Pellegrino, A. L.; Malandrino, G. Surfactant-Free Synthesis of the Full Inorganic Perovskite CsPbBr3: Evolution and Phase Stability of CsPbBr3 vs CsPb2Br5 and Their Photocatalytic Properties. *ACS Appl. Energy Mater.* **2021**, *4* (9), 9431−9439.
(65) Tang, X.; Han, S.; Zu, Z.; Hu, W.; Zhou, D.; Du, J.; Hu, Z.; Li, S.; Zang, Z. All-Inorganic Perovskite CsPb2Br5Microsheets for Photodetector Application. *Front. Phys.* **2018**, *5*, 69.
(66) Weiss, T. P.; Bissig, B.; Feurer, T.; Carron, R.; Buecheler, S.; Tiwari, A. N. Bulk and Surface Recombination Properties in Thin Film Semiconductors with Different Surface Treatments from Time-Resolved Photoluminescence Measurements. *Sci. Rep.* **2019**, *9* (1), 5385.
(67) Kober-Czerny, M.; Dasgupta, A.; Seo, S.; Rombach, F. M.; McMeekin, D. P.; Jin, H.; Snaith, H. J. Determining Parameters of Metal-Halide Perovskites Using Photoluminescence with Bayesian Inference. *PRX Energy* **2025**, *4* (1), 013001.
(68) Caputo, M.; Cefarin, N.; Radivo, A.; Demitri, N.; Gigli, L.; Plaisier, J. R.; Panighel, M.; Di Santo, G.; Moretti, S.; Giglia, A.; et al. Electronic Structure of MAPbI3 and MAPbCl3: Importance of Band Alignment. *Sci. Rep.* **2019**, *9* (1), 15159.
(69) Fan, P.; Gu, D.; Liang, G.-X.; Luo, J.-T.; Chen, J.-L.; Zheng, Z.-H.; Zhang, D.-P. High-Performance Perovskite CH3NH3PbI3 Thin Films for Solar Cells Prepared by Single-Source Physical Vapour Deposition. *Sci. Rep.* **2016**, *6* (1), 29910.
(70) Elsayed, M. R. A.; Elseman, A. M.; Abdelmageed, A. A.; Hashem, H. M.; Hassen, A. Green and Cost-Effective Morter Grinding Synthesis of Bismuth-Doped Halide Perovskites as Efficient Absorber Materials. *J. Mater. Sci.: Mater. Electron.* **2023**, *34* (3), 194.
(71) Elsayed, M. R. A.; Elseman, A. M.; Abdelmageed, A. A.; Hashem, H. M.; Hassen, A. Synthesis and Numerical Simulation of Formamidinium-Based Perovskite Solar Cells: A Predictable Device Performance at NIS-Egypt. *Sci. Rep.* **2023**, *13* (1), 10115.
(72) Li, J.; Han, Z.; Liu, J.; Zou, Y.; Xu, X. Compositional Gradient Engineering and Applications in Halide Perovskites. *Chem. Commun.* **2023**, *59* (35), 5156−5173.
(73) Solis-Ibarra, D.; Smith, I. C.; Karunadasa, H. I. Post-Synthetic Halide Conversion and Selective Halogen Capture in Hybrid Perovskites. *Chem. Sci.* **2015**, *6* (7), 4054−4059.
(74) Zhang, H.; Liao, Q.; Wang, X.; Hu, K.; Yao, J.; Fu, H. Controlled Substitution of Chlorine for Iodine in Single-Crystal Nanofibers of Mixed Perovskite MAPbI3−xClx. *Small* **2016**, *12* (28), 3780−3787.
(75) Yue, H.; Song, D.; Zhao, S.; Xu, Z.; Qiao, B.; Wu, S.; Meng, J. Highly Bright Perovskite Light-Emitting Diodes Based on Quasi-2D Perovskite Film through Synergetic Solvent Engineering. *RSC Adv.* **2019**, *9* (15), 8373−8378.
(76) Laxmi, L.; Kabra, D. Optimization of Composition with Reduced Phase Impurity in Quasi-2D Perovskite for Electroluminescence. *Adv. Photonics Res.* **2021**, *2* (6), 2000164.
(77) Han, D.; Imran, M.; Zhang, M.; Chang, S.; Wu, X.; Zhang, X.; Tang, J.; Wang, M.; Ali, S.; Li, X.; Yu, G.; Han, J.; Wang, L.; Zou, B.; Zhong, H. Efficient Light-Emitting Diodes Based on in Situ Fabricated FAPbBr3 Nanocrystals: The Enhancing Role of the Ligand-Assisted Reprecipitation Process. *ACS Nano* **2018**, *12* (8), 8808−8816.
(78) Jarmouni, N.; Tomaiuolo, M.; Gabbani, A.; Genovese, D.; Pineider, F.; Bassam, R.; Belaaouad, S.; Benmokhtar, S. Low Temperature Synthesis of Ultra-Green Luminescent Colloidal FAPbBr3 Perovskite Nanocrystals. *Mater. Today: Proc.* **2022**, *58*, 1480−1484.
(79) Li, X.; Xue, Z.; Luo, D.; Huang, C.; Liu, L.; Qiao, X.; Liu, C.; Song, Q.; Yan, C.; Li, Y.; Wang, T. A Stable Lead Halide Perovskite Nanocrystals Protected by PMMA. *Sci. China Mater.* **2018**, *61* (3), 363−370.
(80) Protesescu, L.; Yakunin, S.; Bodnarchuk, M. I.; Bertolotti, F.; Masciocchi, N.; Guagliardi, A.; Kovalenko, M. V. Monodisperse Formamidinium Lead Bromide Nanocrystals with Bright and Stable Green Photoluminescence. *J. Am. Chem. Soc.* **2016**, *138* (43), 14202−14205.
(81) Caprioglio, P.; Stolterfoht, M.; Wolff, C. M.; Unold, T.; Rech, B.; Albrecht, S.; Neher, D. On the Relation between the Open-Circuit Voltage and Quasi-Fermi Level Splitting in Efficient Perovskite Solar Cells. *Adv. Energy Mater.* **2019**, *9* (33), 1901631.

https://doi.org/10.1021/acsnano.5c10397
ACS Nano 2025, 19, 30428−30440